

# Observation of Solar Wind Charge Exchange Emission from Exospheric Material in and outside Earth's Magnetosheath

## May 14, 2008

S. L. Snowden,<sup>1,2</sup> M. R. Collier,<sup>3</sup> T. Cravens,<sup>4</sup> K. D. Kuntz,<sup>5</sup> S. T. Lepri,<sup>6</sup> I. Robertson<sup>4</sup>  
and  
L. Tomas<sup>7</sup>

### ABSTRACT

A long *XMM-Newton* exposure is used to observe solar wind charge exchange (SWCX) emission from exospheric material in and outside Earth's magnetosheath. The light curve of the O VII (0.5–0.62 keV) band is compared with a model for the expected emission, and while the emission is faint and the light curve has considerable scatter, the correlation is significant to better than 99.9%. This result demonstrates the validity of the geocoronal SWCX emission model for predicting a contribution to astrophysical observations to a scale factor of order unity (1.36). The results also demonstrate the potential utility of using X-ray observations to study global phenomena of the magnetosheath which currently are only investigated using *in situ* measurements.

*Subject headings:* X-rays: general, X-rays: ISM, solar system: general, interplanetary medium, (Sun:) solar wind

### 1. Introduction

Diffuse X-ray emission from the solar system has been observed for several decades as an unidentified contamination component in observations of the soft X-ray background. It was seen in the Wisconsin sounding-rocket survey data as offsets between overlapping parts of adjacent fields (McCammon et al. 1983; Burrows 1982), and in the HEAO-1 A2 maps (Garmire et al. 1992) as

striping. However, it was during the *ROSAT* All-Sky Survey (RASS, Snowden et al. 1995, 1997) that the insidious nature of the solar system emission became clear, even if the source was not yet identified. The RASS data had considerably better statistics and coverage than previous surveys allowing the striping to be much more obvious. The contamination is clearly visible in the uncleaned maps of the  $\frac{1}{4}$  keV band (Figure 1, upper panel). At the time the source of the striping was unknown and was treated empirically by modeling it as a temporally-varying flat field and then subtracting it from the data (Figure 1, lower panel). In practice this worked relatively well although some residual striping remained. For lack of a better identification and because of the typical relative durations (e.g., compared to auroral X-rays which had durations of order 10 minutes), the count-rate excesses responsible for the striping were referred to as “long-term enhancements” (LTEs, Snowden et al. 1994, 1995).

*ROSAT* pointed observations were also often affected by this contamination and methods were developed to subtract them from images (Snow-

---

<sup>1</sup>Code 662, NASA/Goddard Space Flight Center, Greenbelt, MD 20771

<sup>2</sup>Steven.L.Snowden@nasa.gov

<sup>3</sup>Code 673, NASA/Goddard Space Flight Center, Greenbelt, MD 20771

<sup>4</sup>Department of Physics and Astronomy, University of Kansas, Lawrence, Kansas

<sup>5</sup>Henry A. Rowland Department of Physics and Astronomy, The Johns Hopkins University, 366 Bloomberg Center, 3400 N. Charles Street, Baltimore, MD 21218

<sup>6</sup>Department of Atmospheric, Oceanic, and Space Sciences, The University of Michigan, Ann Arbor, MI.

<sup>7</sup>European Space Astronomy Centre, European Space Agency, P.O. Box 78, Villanueva de la Caada, 28691 Madrid

den et al. 1994). One such observation is of particular interest, a pointing at the Moon (Schmitt et al. 1991). The surface brightness of the dark side of the moon (the observation was done when the Moon was half full) was well above the level expected from known sources, and Schmitt et al. (1991) suggested that the excess emission was bremsstrahlung from solar-wind electrons impinging on the surface. However, comparing the off-Moon intensity of the observation with the cleaned RASS data showed a significant excess likely due to an LTE. In addition, the enhancement was roughly equal to the surface brightness of the dark Moon, which suggests a cis-lunar origin for the LTEs.

The study of diffuse X-ray emission from the solar system gained interest with the detection of X-rays from comets (e.g., Lisse et al. 1996). After some discussion as to the origin of the X-rays (e.g., scattered solar X-rays were considered and then ruled out) it was eventually determined that solar wind charge exchange (SWCX) was responsible (Cravens 1997). SWCX occurs when a highly charged ion of the solar wind interacts with a neutral atom and picks up an electron in a highly excited state. The excited ion then decays to a lower energy state emitting a photon with a characteristic energy of the ion.

SWCX was subsequently suggested as the source mechanism for the LTEs observed in the RASS as well as *ROSAT* pointed observations (Cox 1998; Cravens 2000). Because of the time scales of their temporal variability measurable by *ROSAT* (a few days or less) the location of the LTE production is likely to be relatively local in the solar system; either from near Earth's magnetosheath or within the nearest few AU from Earth.

SWCX has been observed by *Chandra* (e.g., during a dark moon observation, Wargelin et al. 2004), *XMM-Newton* (e.g., during an observation of the *Hubble* Deep Field North, HDFN, Snowden, Collier, & Kuntz 2004, hereafter SCK04), and *Suzaku* (e.g., during an observation of the north ecliptic pole, Fujimoto et al. 2007). While the SWCX emission observed by *Chandra* clearly must originate in the near-Earth environment as the pointing was at the dark Moon, that need not be the case for the *XMM-Newton* and *Suzaku* observations. Figure 1 of SCK04 displays the time

variation of the X-ray emission, solar wind flux, and oxygen ionization state ratios for that observation while their Figures 2 and 3 show the observed spectrum of the SWCX emission. The spectrum shows strong lines of O VII and O VIII, as well as lines from C VI, Ne IX, and Mg XI, all of which are also lines of astrophysical interest. The 0.52-0.75 keV band light curve has a nearly constant rate until a strong solar wind enhancement (as measured by the *ACE* spacecraft) passes the earth, and as the solar wind flux and ionization state (as measured by the  $O^{+7}/O^{+6}$  ratio) drop, so does the X-ray count rate. On one hand, the nearly contemporaneous cutoff suggests a near-Earth origin for the SWCX. On the other hand, the nearly constant count rate before the drop, in spite of the large parameter variations, suggests otherwise. Distributing the SWCX emission over a longer path length along the line of sight could smooth out the light curve, however Collier et al. (2005a) demonstrate that the emission would still have to originate over a small fraction of an AU. The same event has been modeled as due to a large scale heliospheric structure (Koutroumpa et al. 2006), but the bulk of the variation is due to local emission. On the third hand, the *XMM-Newton* observation geometry was serendipitously good for observing SWCX emission from near the sub-solar point of Earth's magnetosheath. This is the region of maximum exospheric emission (Robertson & Cravens 2003), which again suggests a very local origin.

Although the event described by SCK04 portrayed the full scale of the problem of the time-variable SWCX emission, it was not clear whether the emission was due primarily to the solar wind interaction with exospheric material in and just outside the magnetosheath (a large emissivity over a fairly short path-length) or whether the emission was primarily due to the solar wind interaction with neutral material in the heliosphere (a smaller emissivity over a much longer path-length). An archival study of sets of repeated *XMM-Newton* observations of the same target showed that time variable SWCX can be a problem even when one is not observing near the sub-solar point of the magnetosheath, provided that the solar wind flux is relatively high (Kuntz & Snowden 2008a). This is made clear by *ROSAT* and *Suzaku* observations being affected by SWCX as both observatories were/are only able to observe through the flanks

of the magnetosheath. (Both satellites had/have orbits with altitudes of 550–600 km and were constrained to observe within a range of  $\sim \pm 20^\circ$  from the perpendicular to the Earth-Sun line.) However, the Kuntz & Snowden (2008a) study did not resolve the question of the importance of the magnetospheric origin of the time variable SWCX.

For the fifth *XMM-Newton* Announcement of Opportunity (AO-5) we proposed for and received a 100 ks time critical observation (composed of both Guest Observer and calibration time) allowing us to set the geometry of the pointing to maximize the observed flux from the magnetosheath. Despite our best endeavors, and the sterling efforts of the *XMM-Newton* Science Operations Center (SOC), we were unable to schedule an enhancement of the solar wind flux at the time of the observation to improve our statistics. However, even with a moderate solar wind flux we were able to identify a significant correlation between the O VII count rate and our model for SWCX emission from the near-Earth environment. We were also able to use the observation to extract the line intensities for O VII and O VIII emission by spectral fitting.

The goal of this observation was to verify and calibrate our model for SWCX emission from exospheric material in or outside Earth’s magnetosheath in order to better model and predict what, for astrophysical observations, is occasionally a significant background component. This significance was recently made very clear by the case of the disappearing warm-hot intergalactic medium (WHIM) near the Coma cluster. Finoguenov, Briel, & Henry (2003) identified excess O VII, O VIII, and Ne IX emission in one observation of the many *XMM-Newton* Coma Cluster observations, and this excess emission was attributed to the WHIM. However, a recent paper by Takei et al. (2008) using *Suzaku* data from the same direction on the sky show no evidence for the excess emission. While the solar wind was in a relatively quiescent state during the *XMM-Newton* observation we note that the observation geometry was similar to the 2001 HDFN observation of SCK04 which showed very strong SWCX emission.

Section 2 of this paper describes the X-ray data, observation geometry, and *ACE* solar-wind data, § 3 describes our model for the magnetosheath and near-Earth SWCX emission, § 4 describes our

analysis, and § 5 discusses our results and conclusions.

## 2. Data and Observation Geometry

### 2.1. X-ray Data

The X-ray data used for this study came from a single continuous observation obtained with *XMM-Newton* (Jansen et al. 2001; Ehle et al. 2005) during AO-5, ObsID 0402530201. Table 1 contains the observation and line-of-sight (LOS) details. The observation took place on 2006 June 4-5 and lasted  $\sim 96.4$  ks. The European Photon Imaging Camera (EPIC) detectors (Turner et al. 2001) were operated in their Full-Frame (MOS1 and MOS2) and Extended Full Frame (pn) modes with medium filters for the MOS detectors and the thin filter for the pn. The observation was relatively unaffected by the soft-proton background (see Kuntz & Snowden 2008a). The data were processed with *XMM-Newton* Science Analysis Software (SAS<sup>1</sup>) Version 7.1.2 using the Current Calibration Files (CCF) available on 2008 March 12.

The data were reduced using the methods outlined in Snowden et al. (2008), which included running the tasks *emchain* and *epchain* to create calibrated photon event files for the EPIC MOS and pn detectors, respectively. *espfilt* was used to filter the data to remove times of soft-proton contamination for the spectral analysis. Figure 2 shows the MOS1 *espfilt* diagnostic plot with the 2.5–12.0 keV light curve from the field of view (FOV), the 2.5–12.0 keV light curve from the unexposed pixels (pixels in the corners of the detector that are not exposed to the sky), and the histogram of the values in the FOV light curve. The diagnostic plots for the MOS2 and pn instruments are very similar. Spectra were extracted from the entire FOV of the MOS data after removing point sources detected to a uniform limit of  $2 \times 10^{-15}$  ergs cm<sup>-2</sup> s<sup>-1</sup> and data from CCDs operating in an anomalous state (Kuntz & Snowden 2008a). For each point source, the excluded region contains 90% of the emission due to the source, so the size of the excluded region varies with the source’s intensity and distance from the optical

<sup>1</sup>[http://xmm.esac.esa.int/external/xmm\\_sw\\_cal/sas\\_frame.shtml](http://xmm.esac.esa.int/external/xmm_sw_cal/sas_frame.shtml)

axis. The XMM-ESAS<sup>2</sup> software (Snowden & Kuntz 2006; Snowden et al. 2008) was used to create model quiescent particle background spectra (Kuntz & Snowden 2008a). We did not extract a spectrum from the EPIC pn data as we have not yet developed a suitable background model for that detector.

We used data from all three instruments for the light-curve analysis. We extracted light curves in the energy ranges 0.50–0.61 keV (for an O VII band) and 2.5–12.0 keV (a soft-proton monitoring band) from the MOS1 and MOS2 detectors and light curves in the 0.45–0.65 keV and 2.5–12.0 keV bands were extracted from the pn (the broader O VII band for the pn was required by the slightly lower energy resolution). Scatter plots were created of the O VII band versus the hard band (Figure 3). For all of the detectors the bulk of the data points are strongly clumped, while the outliers are linearly correlated. Since the soft proton spectrum has a roughly power-law spectral shape affecting the entire *XMM-Newton* EPIC energy range, this linear correlation implies that the outliers are due to increased soft proton contamination. The count rates from all detectors were added together after excluding the outliers, i.e., those points not in the clumps in Figure 3. Only time periods with accepted count rates from all three detectors were included in the light-curve analysis.

## 2.2. Observation Geometry

The geometry for this observation had several constraints. First, in order to maximize the observed SWCX emission from the magnetosheath, the look direction was required to sweep through the subsolar point, which is about 10  $R_e$  (Earth radii) toward the Sun along the Earth-Sun line during typical solar wind conditions. The sweeping was accomplished by fixing the pointing direction for the observation so that the motion of the satellite in its orbit would properly position the line of sight so it cut through the magnetosheath in the desired manner. Because *XMM-Newton*'s apogee distance is also  $\sim 10 R_e$  and *XMM-Newton* is only able to point within  $\pm 20^\circ$  of the perpendicular from the Earth-Sun line, we required an observation date for which the apogee was near the Earth-Sun line (early June). While there was

no reason to point at any specific position on the sky, in order to maximize the ratio of the SWCX emission to the cosmic background we needed to choose a direction on the sky where the cosmic background is faint in the  $\frac{3}{4}$  keV band.

After a somewhat painful period of trial and error we were able to find an orbit and look direction which satisfied the constraints; revolution (orbit) #1188, 2006 June 4–5 with  $\alpha = 22^h 19^m 45.30^s$ ,  $\delta = +72^\circ 26' 22.0''$ . The Galactic column density of H I in this direction is  $\sim 3 \times 10^{21} \text{ cm}^{-2}$  and the RASS  $\frac{3}{4}$  keV count rate is  $\sim 8 \times 10^{-5} \text{ counts s}^{-1} \text{ arcmin}^{-2}$ , a very low count rate. The RASS  $\frac{1}{4}$  keV emission is also quite low in this direction. Figures 4 and 5 detail the observation geometry of the satellite location and look direction relative to the magnetosheath.

## 2.3. The Solar Wind and ACE Data

The solar wind, a partially ionized plasma continually flowing from the Sun, contains on average about 96% protons, 4% alpha particles, and less than one percent heavier highly charged species. Solar wind densities are typically  $\sim 5 \text{ cm}^{-3}$  and the magnetic field strength is about 7 nT. However, solar wind properties are highly time variable, and over the approximately eleven year solar cycle the solar wind flux goes from an average of about  $3.2 \times 10^8 \text{ cm}^{-2} \text{ s}^{-1}$  at solar minimum to about  $4.8 \times 10^8 \text{ cm}^{-2} \text{ s}^{-1}$  at solar maximum, while the solar wind speed goes from about  $390 \text{ km s}^{-1}$  at solar minimum to  $530 \text{ km s}^{-1}$  at solar maximum (Rucinski et al. 1996). The solar wind tends to be highly structured with scale lengths as short as tens of Earth radii in both the magnetic field (Collier et al. 1998) and plasma (Richardson & Paularena 2001). At the nominal flow speed of about  $450 \text{ km s}^{-1}$ , the solar wind takes almost four days to flow from the Sun to the Earth and over a year to arrive at the termination shock at  $\sim 100 \text{ AU}$ .

Spacecraft such as the Advanced Composition Explorer (*ACE*, Stone et al. 1998) and Wind (Acuña et al. 1995) monitor the solar wind from the L1 point, a point about 235 Earth radii upstream where the gravitational force between the Earth and Sun balance. Because spacecraft at L1 typically have halo orbits around this point with a radius of about 40 Earth radii, the *in-situ* observations made by upstream monitors may not

<sup>2</sup>[http://xmm.gsfc.nasa.gov/docs/xmm/xmmhp\\_xmmesas.html](http://xmm.gsfc.nasa.gov/docs/xmm/xmmhp_xmmesas.html)

reflect the exact properties of the solar wind that impacts Earth (or another spacecraft) and there is a non-negligible lag ( $\sim 1$  hour between L1 and the Earth.)

The small fraction of heavy high charge-state ions in the solar wind produces the soft X-ray emission from SWCX. Unfortunately, because of their low abundance in the solar wind, measurements of these minor ion species require special instrumental techniques (e.g., Gloeckler et al. 1995), and so are more limited than measurements of the proton and alpha particle densities, flow speeds, and temperatures.

During solar minimum, when most *XMM-Newton* observations have occurred, the solar wind as observed at Earth has shown a periodic structure, oscillating between fast polar coronal hole flow and slower interstream flow as the Sun and its solar dipole rotate. This behavior is relatively typical for observations near solar minimum. At the time of the *XMM-Newton* observation, as shown in Figure 6, the solar wind flux measured by the *ACE* spacecraft was usually below its nominal flux of  $3 \times 10^8 \text{ cm}^{-2} \text{ s}^{-1}$ . The two-hour-averaged  $\text{O}^{+7}$  flux, also from *ACE*, showed relatively typical values. In short, this was a calm solar wind time period.

To give a perspective on the solar wind fluxes during the time of the X-ray observation, Figure 7 shows the integral histograms of the solar wind proton and  $\text{O}^{+7}$  fluxes for the year 2006. The range of proton fluxes were typical for the year while on average the  $\text{O}^{+7}$  fluxes were slightly elevated.

### 3. Magnetosheath SWCX Emission Model

SWCX emission is due to the transfer of an electron from a neutral atom, usually H or He, to an excited state in a heavy solar wind ion, and the subsequent radiative decay. Given the ionization states in the solar wind, the resultant photons are typically in the extreme UV or soft X-ray region of the spectrum. Following Cravens (2000) we define the photon production rate (emissivity) for a given line as:

$$P_X = \alpha n_{sw} n_n \langle g \rangle \quad (1)$$

where  $n_{sw}$  is the density of the solar wind protons,  $n_n$  is the density of the neutral “donor” atoms, and

$\langle g \rangle$  is their relative velocity. The scale factor  $\alpha$  contains the abundance of the solar wind ion of interest, the branching ratios in the radiative decay, and the interaction cross-section, which depends upon the relative velocity, and the donor species. For hydrogen and for medium solar wind activity, a reasonable value for an  $\alpha$  appropriate for a broad X-ray band with  $E > 100 \text{ eV}$  is  $6 \times 10^{-16} \text{ eV cm}^2$  (Pepino et al. 2004), and for helium the value is about half that of hydrogen.

The total X-ray emission observed from a specific line of sight is given by

$$4\pi I = \int_{s=0}^{s=\infty} P_X(s) ds \quad (2)$$

where  $s$  is the position along the line of sight. The interval over which one needs to integrate is set by the phenomena producing the emission.

For a line of sight originating from a spacecraft in earth orbit there are two sources of neutral donor atoms. The first is the extended geocorona, the outermost, most tenuous part of the atmosphere, which is composed almost entirely of hydrogen. The geocoronal neutral densities are obtained from the Hodges (1994) model of the terrestrial exospheric hydrogen density. This model is tabulated to  $9.7 R_E$ , where the structure is fairly smooth; we have extrapolated the model at higher  $R$  with a  $R^{-3}$  distribution. The second source of donor atoms, which is spatially quite complex, is the neutral interstellar medium which streams through the heliosphere. The interstellar medium is comprised primarily of H and He where the density of He is about 10% that of H in the local interstellar cloud (LIC) which surrounds the heliosphere (Gloeckler & Geiss 2001; Gloeckler et al. 2004). The interstellar medium within the heliosphere is initially the same but is strongly affected by the Sun. As interstellar atomic hydrogen approaches the Sun it experiences both the attractive force of gravity ( $\propto r^{-2}$ ) and the repulsive force of radiation pressure (also  $\propto r^{-2}$ ). This creates a hydrogen cavity around the Sun with a radius (at the 10% density level) of a few AU in the up-interstellar-wind direction ( $\lambda, \beta \sim 254^\circ \pm 3^\circ, 7^\circ \pm 3^\circ$ ) to  $\sim 10 - 15 \text{ AU}$  in the downstream direction (Quemerais, Lallement, & Bertaux 1993). Because hydrogen is also ionized as it approaches the Sun, its upwind density is significantly greater than its downwind den-

sity. Neutral helium is also depleted near the Sun due to photoionization, however because the cross sections for helium are significantly smaller than those for hydrogen, helium can be found much closer to the Sun than hydrogen. Further, as neutral helium passes the Sun, it is gravitationally focused, substantially increasing its density in the downwind helium-focusing cone. We have derived the interstellar neutral densities from the Fahr “hot” model (Fahr 1971, 1974).

There are two important regimes for solar wind ion-neutral interactions. The first is the magnetosheath, the region directly behind the Earth’s bowshock. The bowshock brakes the solar wind, increasing the density of the solar wind in the “nose” of the bowshock by roughly a factor of four, and by lower factors along the “flanks” of the bowshock. Since the nose of the magnetosheath is also the place where the bowshock is the closest to the Earth, this is also the magnetosheath region with the highest neutral density, and thus the region expected to have the greatest SWCX emission. The solar wind parameters (density, speed, and temperature) inside the magnetosheath are given by the Spreiter, Summers, & Alksne (1966) numerical global hydrodynamic model. The second regime of interest is the free space outside of the bowshock. Here there is still a significant density of geocoronal hydrogen as well as the free-flowing interstellar medium.

The nose of the magnetopause is at  $\sim 9.7 R_E$  under nominal solar wind conditions, and that distance varies with the solar wind ram pressure as  $(n_{sw}u_{sw}^2)^{-\frac{1}{6}}$ , where  $u_{sw}$  is the solar wind speed. Because the exospheric density drops off as  $R^{-3}$  where  $R$  is distance from the center of the Earth, the exospheric neutral density at the nose of the magnetopause varies as  $\sim R^{-3} \sim (n_{sw}u_{sw}^2)^{-\frac{1}{2}}$ . The soft X-ray emission scales with the product of the exospheric neutral density and the solar wind flux,  $n_{sw}u_{sw}$ , so that the soft X-ray emission goes as  $\sim n_{sw}u_{sw}(n_{sw}u_{sw}^2)^{-\frac{1}{2}} = n_{sw}^{\frac{3}{2}}u_{sw}^2$ . The emission responds non-linearly to both increases in solar wind density and solar wind speed varying almost as the square of the solar wind flux. With this observation taking place during a relative lull in the solar wind, the expected SWCX emission is also relatively low.

We have integrated our model for the interac-

tion of the solar wind with the geocoronal neutral material, including the interactions in the magnetosheath to a distance of  $50 R_E$ . We have integrated our model for the interaction of the solar wind with the interstellar material to a distance of 200 AU; essentially encompassing the entire path length through the heliosphere.

The solar wind conditions enter our model not only through the  $n_{sw}$  in Equation 1 and through the  $\alpha$  in Equation 1, which depends on the velocity and temperature of the solar wind, but also through the Spreiter, Summers, & Alksne (1966) model of the magnetosheath since the size and shape of the magnetosheath depends upon the strength of the solar wind. We have modeled the solar wind as a series of spherical fronts emanating from the Sun. The solar wind proton density, speed, and temperature for each front was derived from the OMNIWeb<sup>3</sup> archive. The data extracted from OMNIWeb (King & Papitashvili 2004) had a time resolution of one hour, and the data were time shifted to the location of the bowshock. The proton thermal velocity was derived from the proton temperature using

$$v_{th} = \sqrt{3k_B T / m_p}, \quad (3)$$

where  $m_p$  is the proton mass and  $T$  is the proton temperature, while the total average proton speed was calculated using

$$\langle g \rangle = \sqrt{v_{th}^2 + u_{sw}^2} \quad (4)$$

where  $u_{sw}$  is the measured average proton speed.

As discussed above, the interaction of the solar wind with the magnetosheath causes magnetosheath to expand and contract. With each time step we scale the Spreiter, Summers, & Alksne (1966) model of the magnetosheath to the size appropriate for the solar wind flux in that time step, and then integrate the emissivity along the line of sight. Given the limitations of the solar wind data, we assume nearly planar propagation near the earth and a uniform pressure across the nose of the magnetosheath. Such treatment is valid given the time-scales involved; due to low count rates the X-ray data require a time binning of 15 minutes to achieve a reasonable significance while the

<sup>3</sup><http://omniweb.gsfc.nasa.gov/>

time required for a solar wind front to move from the nose of the magnetosheath to the level of the earth is only about three minutes. Thus, much of the dynamic nature of the magnetosheath will be averaged out by the time-binning forced by the X-ray data.

## 4. Analysis

### 4.1. Light Curve

In this part of the analysis we consider the O VII light curve and test for any correlation between the model and the observed count rate. The O VII band was chosen as O VII dominates the SWCX emission for most observations in the *XMM-Newton* bandpass. The narrow band was selected in order to maximize the signal-to-noise for the analysis. Note that since the O VII light curve was constructed from all of the counts in 0.5-0.61 keV (MOS) or 0.45-0.65 keV (pn) band, the O VII light curve also contains a contribution from adjacent spectral bands (due to the finite energy resolution of the detectors) as well as the underlying spectral continuum. Thus, even in the absence of any O VII line emission, the O VII band count rate would not be zero. Figure 8 shows the O VII band count rate which sums the data from all three EPIC instruments. This plot also contains scaled curves of the model rates for the heliospheric SWCX (dot and dashed line) and magnetosheath SWCX (dotted line) emission models in order to show their temporal variation. (The model emission was arbitrarily scaled for display purposes.) The solid curve shows the best-fit model which is a constant (to account for the non-variable component in the O VII band) plus a scaling of the magnetosheath SWCX emission. The model heliospheric emission showed too small a variation over the observation interval to significantly separate it from a constant component. The fit is far from statistically significant with  $\chi^2 = 191$  for 75 degrees of freedom. However, the excessive  $\chi^2$  value appears to be dominated by the short-period scatter rather than global deviations of the model. If this is the case, the extra scatter could possibly be accounted for by additional variation in the  $O^{+7}$  flux relative to the solar wind proton flux which is used in the model. Because the heavier ions have much lower abundances the *ACE* solar wind data can achieve reasonable statistics

only by integrating over longer time intervals. For  $O^{+7}$  this typically requires time intervals greater than an hour.

Since the  $\chi^2$  value for the fit is far from acceptable we use the correlation coefficient to test whether the SWCX model plus a constant can be a reasonable representation of the data. The correlation coefficient is 0.435 for 77 samples, which implies a probability of  $< 0.001$  that the data could be drawn from an uncorrelated distribution (Bevington 1969). To gain more confidence that the correlation is real we considered two additional qualitative tests. First, we calculated the  $\chi^2$  value for a range of scale factors. Figure 9 displays the resultant  $\chi^2$  curve with a delta  $\chi^2$  of  $\sim 50$  between the best-fit value and a zero scaling. Thus, our magnetospheric model is considerably better than a constant model. Similarly, our magnetospheric model must be better than the heliospheric model alone, which is relatively constant.

For the second test we examined the variation of the  $\chi^2$  value when the model time is offset from the data. Figure 10 shows the result of this test with a sharp  $\chi^2$  minimum which is both deep (a delta  $\chi^2$  value of 30-40) and has a time offset consistent with zero. These two tests give us confidence that the correlation is real and that the scaling is well defined.

Before fitting the model to the data it was necessary to scale it to be appropriate for the *XMM-Newton* EPIC detectors for the O VII band. The model is in units of  $\text{keV cm}^{-2} \text{ s}^{-1}$  and so must be scaled by energy of O VII lines ( $\sim 0.562 \text{ keV}$ ) and the area-solid-angle product for the EPIC detectors ( $0.0161 \text{ cm}^{-2} \text{ sr}$ ). After this scaling, the best-fit scale factor for the magnetosheath emission is 1.36, implying that the model underpredicted the SWCX flux by only  $\sim 36\%$ . Although it is not entirely appropriate, we use the  $\chi^2$  curve shown in Figure 9 to get an idea of the uncertainty in the magnetosheath model scale factor. Using a  $\Delta\chi^2 = 2.71$  criteria, which in normal circumstances would be  $1.6\sigma$ , yields an uncertainty of 0.32, for a scale factor of  $1.4 \pm 0.3$ .

The average SWCX O VII emission can be extracted from the fitted light curve, and is  $0.026 \text{ counts s}^{-1}$ . Assuming that the magnetospheric contribution is solely due to the O VII lines, combining this count rate with the area-solid-angle product we find an average intensity of  $1.6 \pm$

0.4 photons  $\text{cm}^{-2} \text{ s}^{-1} \text{ sr}^{-1}$  (hereafter line units, LU), using the same assumption for the uncertainty as above.

## 4.2. Spectral Analysis

Because of the nature of this observation, long, relatively clean, and in a direction with a relatively high Galactic column density, it is a good observation to study the O VII and O VIII emission of the local diffuse X-ray background.

For the spectral analysis we used Xspec to fit the data using a standard model for the emission from the diffuse X-ray background. The model is comprised of an unabsorbed foreground thermal component representing the putative Local Hot Bubble (LHB) emission, an absorbed thermal component, representing emission from the Galactic disk and halo, and a background power law absorbed by the entire Galactic column along the line of sight, representing the unresolved extragalactic background. The absorption of the thermal component was allowed to vary as the absorption and the emission along the LOS may be interleaved. The remaining *XMM-Newton* instrumental background was modeled by two lines (Al  $K\alpha$  at 1.49 keV and Si  $K\alpha$  at 1.75 keV) while the residual soft proton contamination was modeled by a power law spectrum not folded through the instrumental response (Kuntz & Snowden 2008a). In order to better constrain the fitted model we used the HEASARC X-ray Background Tool<sup>4</sup> to extract a RASS spectrum for a circular region with a  $1^\circ$  radius around the pointing direction of our observation, which was then simultaneously fit with the *XMM-Newton* data.

APEC<sup>5</sup> models where the relative abundances could be individually set were used for the thermal emission. The abundances for oxygen were set to zero and the rest of the abundances were fixed at 1. Two additional Gaussians were then included to model the O VII emission at 0.56 keV and O VIII emission at 0.65 keV. The data were then fit to determine the oxygen flux. Figure 11 shows the data and the best-fit model. To get a better perspective on the uncertainties in the spec-

tral fit results for the O VII and O VIII lines we used Xspec to create the confidence-contour plot shown in Figure 12.

The fitted values for the fluxes in the O VII and O VIII lines are  $4.3 \pm 0.4$  LU and  $0.39 \pm 0.17$  LU, respectively. This is a marginal detection of O VIII but is significant for O VII. Using the derived value for the magnetosheath SWCX O VII from the light curve analysis of  $1.6 \pm 0.4$  LU, this leaves  $2.7 \pm 0.6$  LU originating either as thermal emission from the LHB or from the heliospheric SWCX.

The  $\ell = 111^\circ$  ( $\ell, b \sim 111.14^\circ, 1.11^\circ$ ) line of sight described in Kuntz & Snowden (2008b) is only  $11.8^\circ$  away from the line of sight described here. For that observation, the line of sight passed through the flanks of the magnetosheath at an angle of  $106^\circ$  from the Earth-Sun line. The solar wind proton flux was also smaller for that observation,  $1.39 \times 10^8 \text{ cm}^{-2} \text{ s}^{-1}$ , and the  $\text{O}^{+7}/\text{O}^{+6}$  abundance ratios were similar for two observations. For the  $\ell = 111^\circ$  line of sight the total O VII emission (summed over all emission components) was  $3.0^{+0.8}_{-0.4}$  LU, which is consistent with our non-magnetosheath measurement. The total O VIII emission in that direction was  $1.6^{+0.3}_{-0.4}$ . However, it should be noted that the RASS R45 band value for the  $\ell = 111^\circ$  LOS is  $50 \pm 6 \times 10^{-6} \text{ counts s}^{-1} \text{ arcmin}^{-2}$ , exceptionally dark due to a molecular cloud shadow, while in our LOS it is  $76 \pm 7 \times 10^{-6} \text{ counts s}^{-1} \text{ arcmin}^{-2}$ . Thus one would have expected the  $\ell = 111^\circ$  LOS to be dimmer by a third if the underlying spectra were the same in both directions; conversely one can attribute the difference to SWCX, though the  $\ell = 111^\circ$  LOS should have had a substantially lower magnetospheric contribution. The most likely explanation is that the Kuntz & Snowden (2008b) observation was unaffected by any significant magnetosheath emission and that the excess O VIII line strength is due to other thermal emission regions along the line of sight in the Galactic disk.

## 5. Results and Conclusions

From our analysis of the X-ray data we derive an average O VII flux of 1.6 LU from the magnetosheath and near-Earth SWCX emission. This is in very good agreement with the model prediction which is 1.2 LU, and provides a very strong validation of our SWCX emission model. The rest of the

<sup>4</sup>High Energy Astrophysics Science Archive Research Center, <http://xmm.gsfc.nasa.gov/cgi-bin/Tools/xraybg/xraybg.pl>

<sup>5</sup>[http://cxc.harvard.edu/atomdb/sources\\_apec.html](http://cxc.harvard.edu/atomdb/sources_apec.html)



observed O VII emission, 2.7 LU, originates foreground to the dark clouds forming the backstop for this observation, and so may originate in the heliosphere, LHB, or farther away in the Galactic disk. This value agrees reasonably well with the 3.0 LU results of Kuntz & Snowden (2008b) and the 3.5 LU local emission of Smith et al. (2007).

Our marginal O VIII result of 0.4 LU is significantly lower than those of Kuntz & Snowden (2008b) but agrees well with the marginal local result of Smith et al. (2007) ( $0.24 \pm 0.10$  LU). This places an upper limit on O VIII SWCX emission from the heliosphere, which should be relatively constant over time, of  $\sim 0.3$  LU.

With a functional model for SWCX emission from the magnetosheath and near-Earth environment it is now possible to identify those astrophysical observations which are likely to be affected by this “contamination” component. With further refinements of the model and additional calibration observations it may be possible to model SWCX emission accurately enough to subtract it from the data.

Another interesting possibility suggested by the success of this project is the remote monitoring of the magnetosheath, magnetopause, and solar wind. In the past, observations of the terrestrial magnetopause have been mainly restricted to *in-situ* observations. The notable exceptions to this are neutral atom imaging (e.g., Taguchi et al. 2004; Collier et al. 2005b) and radio plasma imaging (e.g., Green & Reinisch 2003; Nagano et al. 2003). X-ray imaging, however, may be the best technique for global monitoring of the magnetopause from, for example, a spacecraft positioned off to the side of the Earth in a 1 AU orbit that leads or follows the Earth, viewing nearly perpendicular to the Earth-Sun line (Robertson & Cravens 2003; Robertson et al. 2006). Given that all energy transfer from the solar wind into the magnetosphere must pass through the magnetopause, global imaging of the magnetopause boundary will prove invaluable for space weather studies.

We would like to thank the mission planners at the *XMM-Newton* Science Operations Center (SOC) for their patience and help in the scheduling of this non-standard time-critical observation. We would also like to thank the SOC for the additional Calibration Time that was allocated to the

observation.

This paper was based on an observation obtained with *XMM-Newton*, an ESA science mission with instruments and contributions directly funded by ESA Member States and NASA. The OMNI data were obtained from the GSFC/SPDF OMNIWeb interface. This work was supported by a NASA XMM-Newton GO grants including NNX06AG73G.

## REFERENCES

- Acuña, M. H., Ogilvie, K. W., Baker, D. N., Curtis, S. A., Fairfield, D. H., & Mish, W. H. 1995, *Space Sci. Rev.*, 71, 5
- Bevington, P. R. 1969, *Data Reduction and Error Analysis for the Physical Sciences*, (McGraw-Hill Book Company:New York)
- Burrows, D. N. 1982, Ph.D. Thesis, University of Wisconsin-Madison, Spatial structure of the diffuse soft X-ray background
- Collier, M. R., Slavin, J. A., Lepping, R. P., Szabo, A., & Ogilvie, K. 1998, *Geophys. Res. Lett.*, 25, 2509
- Collier, M. R., Moore, T. E., Snowden, S. L., & Kuntz, K. D. 2005, *Adv. Space Res.*, 35(12), 2157
- Collier, M. R., Moore, T. E., Fok, M.-C., Pilkerton, B., Boardsen, S., Khan, H. 2005, *J. Geophys. Res.*, 110, A02102
- Cox, D. P. 1998, in *The Local Bubble and Beyond*, ed. D. Breitschwerdt, M. J. Freyberg, & J. Trümper (Berlin: Springer), 121
- Cravens, T. E. 1997, *Geophys. Res. Lett.*, 24, 105
- Cravens, T. E. 2000, *ApJ*, 532, L153
- Ehle, M., et al. 2005, *XMM-Newton Users’ Handbook* (Madrid:ESA)
- Fahr, H. J. 1971, *A&A*, 14 263
- Fahr, H. J. 1974, *Sp. Science Rev.*, 15, 483
- Finoguenov, A., Briel, U. G., & Henry, J. P. 2003, *A&A*, 410, 777

- Fujimoto, R., Mitsuda, K., McCammon, D., Takei, Y., Bauer, M., Ishisaki, Y., Porter, S. F., Yamaguchi, H., Hayashida, K., & Yamasaki, N. Y. 2007, *PASJ*, 59(SP1), 133
- Garmire, G. P., Nousek, J. A., Apparao, K. M. V., Burrows, D. N., Fink, R. L., & Kraft, R. P. 1992, *ApJ*, 399, 694
- Gloeckler, G., & Geiss, J. 2001, *AIP Conf. Proc.* 598, *Solar and Galactic Composition*, ed. R. F. Wimmer-Schweingruber (New York: AIP), 281
- Gloeckler, 1995, *Space Sci. Rev.*, 71, 79
- Gloeckler, G., et al. 1998, *SSRv*, 86(1/4), 497
- Gloeckler, G., et al. 2004, *A&A*, 426(3), 845
- Green, J. L., & Reinisch, B. W. 2003, *Space Sci. Rev.*, 109, 183
- Hodges Jr., R. R. 1994, *JGR*, 99, 23, 229
- Jansen, F., Lumb, D., Altieri, B., Clavel, J., Ehle, M., Erd, C., Gabriel, C., Guainazzi, M., Gondoin, P., Much, R., Munoz, R., Santos, M., Schartel, N., Texier, D., & Vacanti, G. 2001, *A&A*, 365, L1
- King, J. H., & Papitashvili, N. E. 2004, *JGR*, 110, A2, A02209, 10.1029/2004JA010804
- Koutroumpa, D., Lallement, R., Kharchenko, V., Dalgarno, A., Pepino, R., Izmodenov, V., & Quémerais, E. 2006, *A&A* 460, 289
- Kuntz, K. D., & Snowden, S. L. 2008a, *A&A*, 478, 575
- Kuntz, K. D., & Snowden, S. L. 2008b, *ApJ*, 674, 209
- Lisse, C. M., et al. 1996, *Science*, 274, 205
- McCammon, D., Burrows, D. N., Sanders, W. T., & Kraushaar, W. L. 1983, *ApJ*, 269, 107
- McComas, D. J., Bame, S. J., Barker, P., Feldman, W. C., Phillips, J. L., Riley, P., & Griffiee, J. W. 1998, *SSRv*, 86(1/4), 563
- Nagano, I., Wu, X.-Y., Takano, H., Yagitani, S., Matsumoto, H., Hashimoto, K., Kasaba, Y. 2003, *J. Geophys. Res.*, 108, 1224
- Pepino R., Kharchenko, V., Dalgarno, A. & Lallement, R. 2004, *ApJ*, 617, 1347
- Plucinsky, P. P., Snowden, S. L., Briel, U. G., Hasinger, G., & Pfeffermann, E. 1993, *ApJ*, 418, 519
- Quemerais, E., Lallement, R., & Bertaux, J.-L. 1993, *J. Geophys. Res.*, 98, 15199
- Richardson, J., & Paularena, K. 2001, *J. Geophys. Res.*, 106, 239
- Robertson, I. P., & Cravens, T. E. 2003, *Geophys. Res. Lett.*, 30(8), 1439
- Robertson, I. P., Collier, M. R., Cravens, T. E. & Fok, M.-C. 2006, *JGR*, 111, A12105
- Rucinski, D., Cummings, A. C., Gloeckler, G., Lazarus, A. J., Mobius, E., & Witte, M. 1996, *Space Sci. Rev.*, 78, 73
- Schmitt, J. H. M. M., Snowden, S. L., Aschenbach, B., Hasinger, G., Pfeffermann, E., Predehl, P., & Trümper, J. 1991, *Nature*, 349, 583
- Smith, R. K. et al. 2007, *PASJ*, 595(SP1), 141
- Snowden, S. L., Collier, M. R., & Kuntz, K. D. 2004, *ApJ*, 610, 1182
- Snowden, S. L., & Freyberg, M. J. 1993, *ApJ*, 404, 403
- Snowden, S. L., Freyberg, M. J., Plucinsky, P. P., Schmitt, J. H. M. M., Truemper, J., Voges, W., Edgar, R. J., McCammon, D., & Sanders, W. T. 1995, *ApJ*, 454, 643
- Snowden, S. L., Egger, R., Freyberg, M. J., McCammon, D., Plucinsky, P. P., Sanders, W. T., Schmitt, J. H. M. M., Trümper, J., & Voges, W. 1997, *ApJ*, 485, 125
- Snowden, S. L., & Kuntz, K. D. 2006, *XMM-Newton* GOF, <ftp://legacy.gsfc.nasa.gov/xmm/software/xmm-esas/xmm-esas.pdf>
- Snowden, S. L., McCammon, D., Burrows, D. N., & Mendenhall, J. A., 1994, *ApJ*, 424, 714
- Snowden, S. L., Mushtozky, R. F., Kuntz, K. D., & Davis, D. S. 2008, *A&A*, 478, 615

- Snowden, S. L., Plucinsky, P. P., Briel, U., Hasinger, G., & Pfeffermann, E. 1992, *ApJ*, 393, 819
- Spreiter, J. R., Summers, A. L., & Alksne, A. Y. 1966, *Space. Sci.*, 14, 223
- Stone, E. C., Frandsen, A. M., Mewaldt, R. A., Christian, E. R., Margolies, D., Ormes, J. F., & Snow, F. 1998, *SSRv*, 86(1/4), 1
- Taguchi, S., Collier, M. R., Moore, T. E., Fok, M.-C., Singer, H. J. 2004, *J. Geophys. Res.*, 109, A04208
- Takei, Y., Miller, E. D., Bregman, J. N., Kimura, S., Ohashi, T., Mitsuda, K., Tamura, T., Yamasaki, N. Y., & Fujimoto, R. (2008), [arXiv:0803.2817](https://arxiv.org/abs/0803.2817)
- Turner, M. J. L. et al. 2001, *A&A*, 365, L27
- Wargelin, B. J., Markevitch, M., Juda, M., Kharchenko, V., Edgar, R. J., & Dalgarno, A. 2004, *ApJ*, submitted

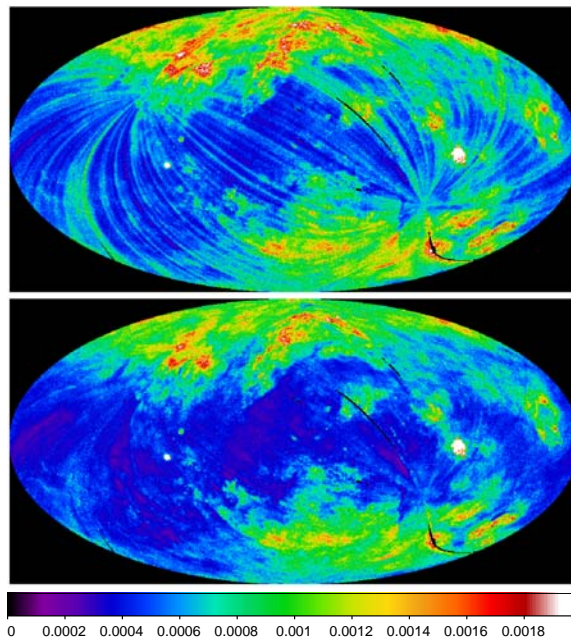


Fig. 1.— RASS maps of the  $\frac{1}{4}$  keV diffuse background before (upper panel) and after (lower panel) removal of the LTEs. The color bar shows the X-ray intensity in units of counts  $\text{s}^{-1} \text{ arcmin}^{-2}$ . The particle background (Snowden et al. 1992; Plucinsky et al. 1993) and scattered solar X-ray background (Snowden & Freyberg 1993) have been subtracted in both maps.

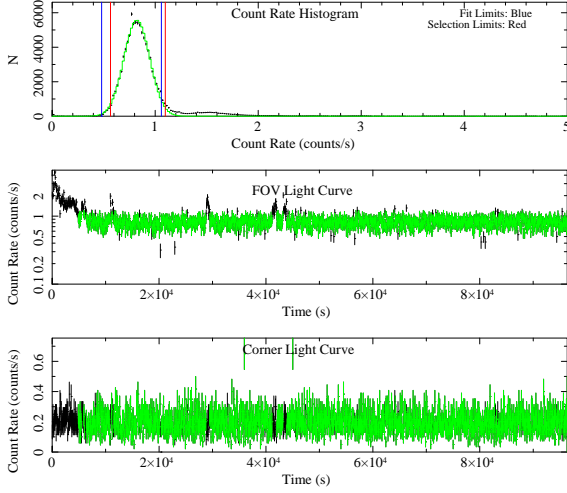


Fig. 2.— MOS1 diagnostic plot from the SAS task *espfilt* with (upper panel) the histogram of the FOV 2.5–12.0 keV light curve, (middle panel) the 2.5–12.0 keV light curve from the FOV, and (lower panel) the 2.5–12.0 keV light curve from the unexposed (to the sky) corners of the detector. Data plotted in green indicate accepted time periods. In the upper panel the vertical blue lines indicate the range over which the histogram data were fitted with a Gaussian. The vertical red lines indicate the count rate range where the data were accepted.

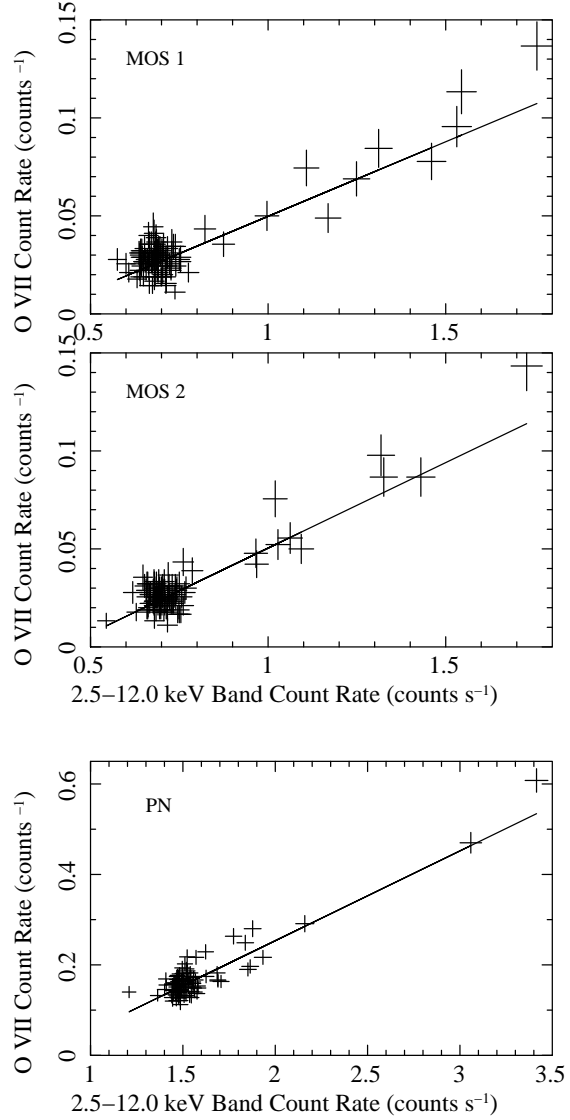


Fig. 3.— O VII band *versus* hard band count rate scatter plots for the MOS1 (upper panel), MOS2 (middle panel), and pn (bottom panel) detectors. The plotted lines show the correlation between the outliers indicating that both the hard band and O VII band are affected in a similar manner, further indicating that they are due to residual soft-proton contamination.

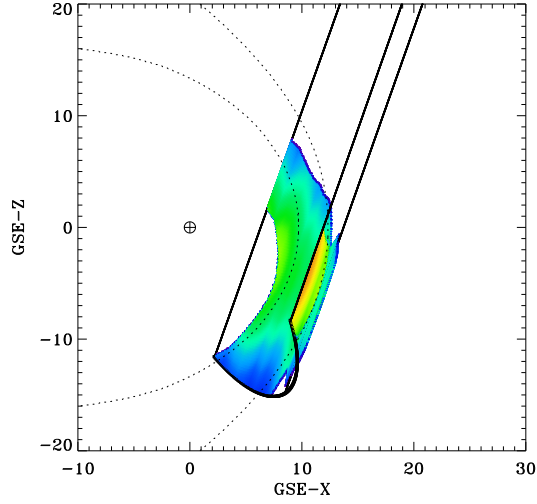


Fig. 4.— Geometry of the observation in the GSE X-Z plane, where X points to the Sun and Z points toward the north ecliptic pole. The curved solid line shows the *XMM-Newton* orbit during the observation while the straight solid lines show the look direction. The dotted lines indicate the rough location of the inner and outer boundaries of Earth's magnetosheath. The colored lines provide a rough estimate of the emissivity ( $n_{sw}n_n\langle g \rangle$ ) within the magnetosheath. The ragged appearance of the boundary of the magnetosheath emission is due the variability in the solar wind strength.

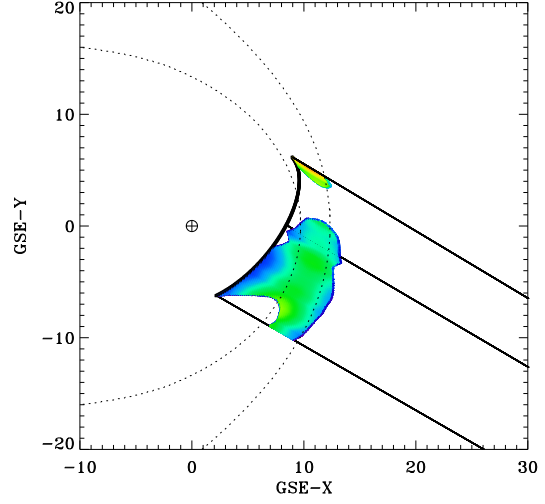


Fig. 5.— Same as Figure 4 except that the projection is in the GSE X-Y plane. The GSE Y axis lies in the ecliptic plane and points opposite to Earth's velocity vector, completing the right-handed coordinate system.

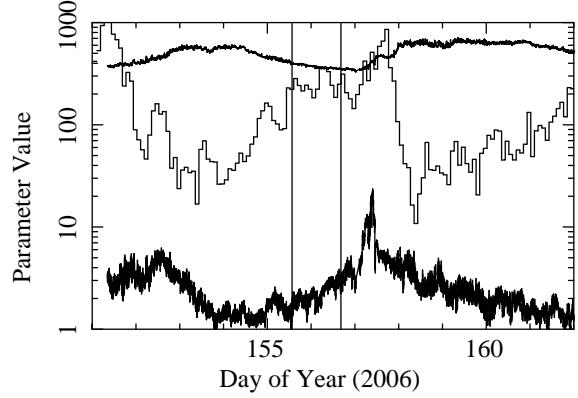


Fig. 6.— *ACE* solar wind data for the observation. The upper curve shows the solar wind proton speed in units of  $\text{km s}^{-1}$  as measured by the SWEPAM instrument (McComas et al. 1998). The middle curve is the  $\text{O}^{+7}$  flux in units of  $10^2$  ions  $\text{cm}^{-2} \text{s}^{-1}$  as measured by the SWICS instrument (Gloeckler et al. 1998). The bottom curve is the solar wind proton flux in units of  $10^8$  protons  $\text{cm}^{-2} \text{s}^{-1}$  as measured by the SWEPAM instrument. The vertical lines show the bounds of the *XMM-Newton* observation.

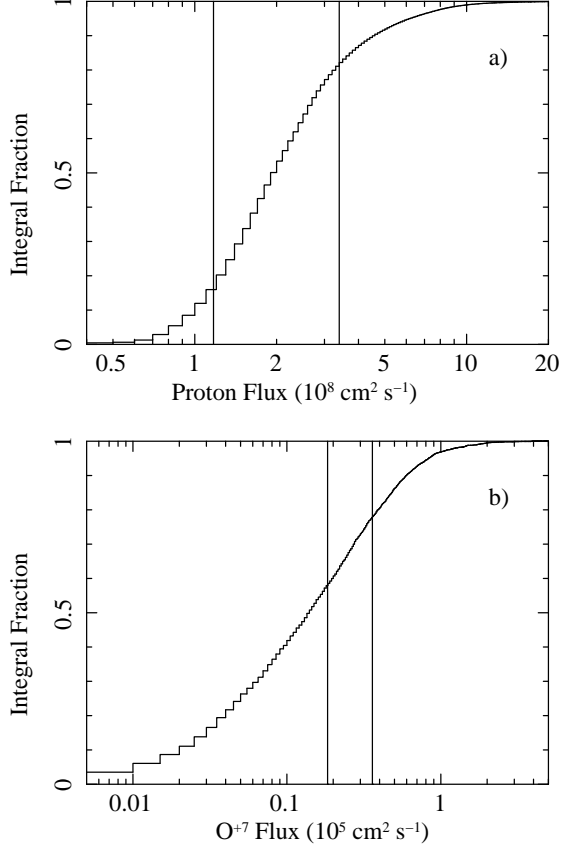


Fig. 7.— Integral histogram of selected *ACE* solar wind data for the year 2006. The upper panel (a) shows the solar wind proton flux in units of  $10^8$  protons  $\text{cm}^{-2} \text{s}^{-1}$  as measured by the SWEPAM instrument. The lower panel (b) shows the solar wind  $\text{O}^{+7}$  flux in units of  $10^5$  ions  $\text{cm}^{-2} \text{s}^{-1}$  as measured by the SWICS instrument. In both panels the vertical lines show the bounds of the ranges experienced during the *XMM-Newton* observation.

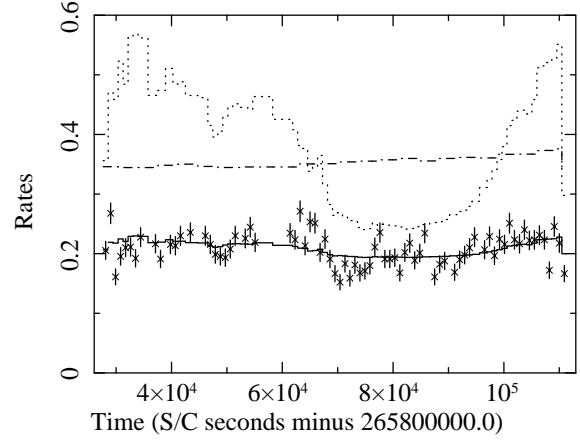


Fig. 8.— O VII light curve (data points with statistical error bars) and other scaled rates for the observation. The solid curve is the best fit model which includes a constant plus a scaling of the magnetosheath and near-Earth model emission (dotted curve). The dotted and dashed curve is a scaled plot of the heliospheric model (SWCX with both hydrogen plus helium) emission. The time binning for the X-ray data is 15 minutes.

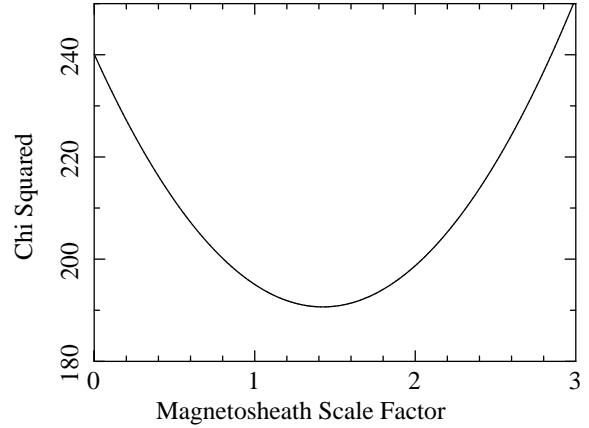


Fig. 9.—  $\chi^2$  value as a function of scale factor for the magnetosheath SWCX emission model.

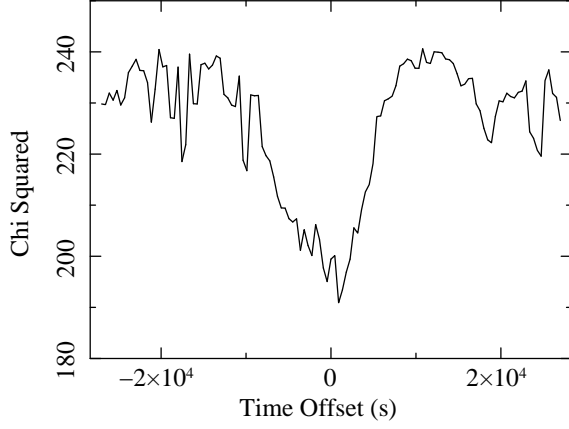


Fig. 10.—  $\chi^2$  value as a function of time shift between the magnetosheath SWCX emission model and data.

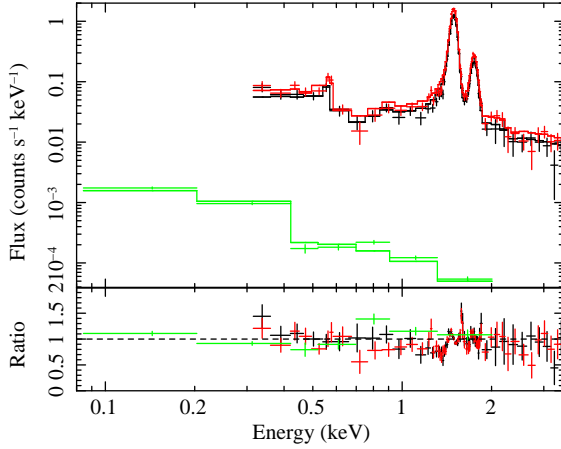


Fig. 11.— Spectral fit for the *XMM-Newton* EPIC MOS (white and red) and RASS (green) spectra. The two lines between 1.5 and 2.0 keV are the Al  $K\alpha$  and Si  $K\alpha$  instrumental lines. The O VII line is at 0.56 keV. The O VIII line is not apparent.

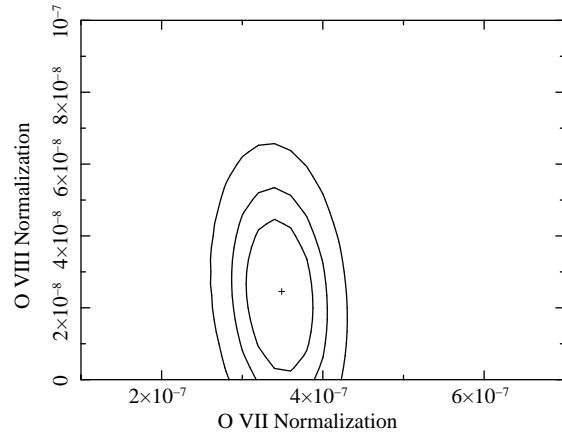


Fig. 12.—  $\chi^2$  contour plot. The axis values are the Xspec normalizations which are in units of  $\text{counts s}^{-1} \text{ arcmin}^{-2}$ . The contours are the 68%, 90%, and 99% confidence values.

TABLE 1  
OBSERVATION DETAILS.

Parameter	Value
ObsID	0402530201
$(\alpha, \delta)$	$22^{\text{hr}} 19^{\text{m}} 45.30^{\text{s}}, +72^{\circ} 26' 22.0''$
$(\ell, b)$	$111.9678^{\circ}, +12.8797^{\circ}$
Start,End Date	2006-06-04 13:32:04,2006-06-05 16:21:11
Total,Good Exposure Time	96.37 ks, 83.34 ks
Galactic H I	$2.9 \times 10^{21} \text{ cm}^{-2}$
RASS R12	$420 \times 10^{-6} \text{ counts s}^{-1} \text{ arcmin}^{-2}$
RASS R45	$78 \times 10^{-6} \text{ counts s}^{-1} \text{ arcmin}^{-2}$